Volume 11
Number 12
28 March 2020
Pages 3113–3380

Chemical Science

rsc.li/chemical-science

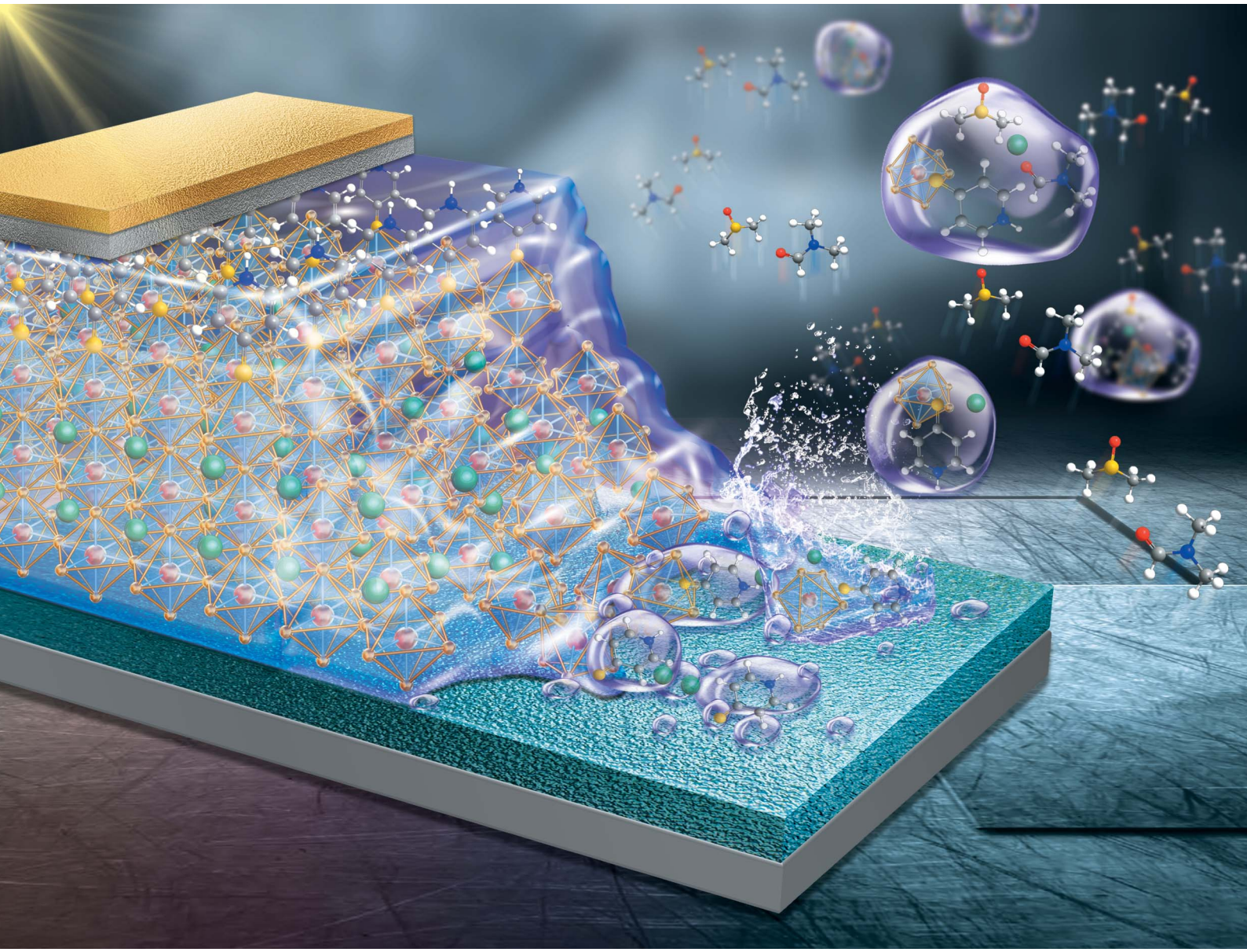

ISSN 2041-6539

ROYAL SOCIETY OF CHEMISTRY

EDGE ARTICLE

Yongzhen Wu *et al.*

Electron-enriched thione enables strong Pb–S interaction for stabilizing high quality $CsPbI_3$ perovskite films with low-temperature processing

Chemical Science

ROYAL SOCIETY OF CHEMISTRY

EDGE ARTICLE

View Article Online
View Journal | View Issue

Cite this: *Chem. Sci.*, 2020, **11**, 3132

All publication charges for this article have been paid for by the Royal Society of Chemistry

Electron-enriched thione enables strong Pb–S interaction for stabilizing high quality $CsPbI_3$ perovskite films with low-temperature processing†

Xiaojia Xu,[a] Hao Zhang,[a] Erpeng Li,[a] Pengbin Ru,[b] Han Chen,[b] Zhenhua Chen,[c] Yongzhen Wu, *[a] He Tian[a] and Wei-Hong Zhu [a]

Cesium lead iodide ($CsPbI_3$) perovskite is a promising photovoltaic material with a suitable bandgap and high thermal stability. However, it involves complicated phase transitions, and black-phase $CsPbI_3$ is mostly formed and stabilized at high temperatures (200–360 °C), making its practical application challenging. Here, for the first time, we have demonstrated a feasible route for growing high quality black-phase $CsPbI_3$ thin films under mild conditions by using a neutral molecular additive of 4(1*H*)-pyridinethione (4-PT). The resulting $CsPbI_3$ thin films are morphologically uniform and phase stable under ambient conditions, consisting of micron-sized grains with oriented crystal stacking. With a range of characterization experiments on intermolecular interactions, the electron-enriched thione group in 4-PT is distinguished to be critical to enabling a strong Pb–S interaction, which not only influences the crystallization paths, but also stabilizes the black-phase $CsPbI_3$ *via* crystal surface functionalization. The 4-PT based $CsPbI_3$ achieves 13.88% power conversion efficiency in a p–i–n structured device architecture, and encapsulated devices can retain over 85% of their initial efficiencies after 20 days of storage in an ambient environment, which are the best results among fully low-temperature processed $CsPbI_3$ photovoltaics.

Received 31st December 2019
Accepted 17th February 2020

DOI: 10.1039/c9sc06574a

rsc.li/chemical-science

Introduction

Although the power conversion efficiency (PCE) of organic–inorganic hybrid perovskite based solar cells (PSCs) has skyrocketed from 3% to a certified 25.2%,[1–5] their intrinsic instability caused by the volatile and hygroscopic properties of the organic cations still remains a major obstacle for practical applications.[6–9] Accordingly, inorganic perovskites that employ cesium (Cs^+) instead of organic cations have attracted considerable interest as an alternative for overcoming the stability issues.[10–12] Among $CsPbX_3$ (X = Cl, Br, and I) perovskites, $CsPbI_3$ is most effective in light harvesting as it exhibits the lowest band gap at around 1.7 eV, which makes it an ideal candidate for application in perovskite/silicon tandem solar cells.[13,14] However, during the fabrication of $CsPbI_3$, it preferentially forms a yellow product (non-perovskite, usually named the δ phase), which is thermodynamically stable and photo-inactive.[15] The conversion of the δ phase to a photo-active black-phase $CsPbI_3$ usually requires a high annealing temperature (higher than 310 °C),[16,17] which makes it incompatible with many thermally sensitive substrates. Moreover, the black-phase $CsPbI_3$ is meta-stable, suffering from spontaneous phase transition to the δ phase at room temperature.[15] Therefore, even though much effort has been made on $CsPbI_3$ based solar cells, their photovoltaic performances still lag behind those of hybrid perovskites.[18–23]

Regarding to these problems, several strategies have been proposed in previous literature reports. For instance, the incorporation of hydriodic acid (HI) or replacing PbI_2 with "$HPbI_3$" in the $CsPbI_3$ precursor solution has been demonstrated to be capable of decreasing the formation temperature of perovskite and improving thin film uniformity.[17,18,24–26] However, this strategy can't eliminate spontaneous phase transition. The modification of the $CsPbI_3$ crystal surface with organic ligands has been reported to be effective to improve the phase stability,[18,24,25] but such post treatments obviously increase the fabrication complexity. Previous studies have also demonstrated that the incorporation of ionic or polymer additives such as sulfobetaine zwitterions,[27] polyvinylpyrrolidone (PVP),[28] and poly (ethylene oxide) (PEO)[29] in $CsPbI_3$ precursor

[a]*Key Laboratory for Advanced Materials and Joint International Research Laboratory of Precision Chemistry and Molecular Engineering, Feringa Nobel Prize Scientist Joint Research Center, Shanghai Key Laboratory of Functional Materials Chemistry, Institute of Fine Chemicals, School of Chemistry and Molecular Engineering, East China University of Science and Technology, Shanghai 200237, China. E-mail: wu.yongzhen@ecust.edu.cn*

[b]*State Key Laboratory of Metal Matrix Composites, Shanghai Jiao Tong University, 800 Dong Chuan Road, Shanghai 200240, China*

[c]*Shanghai Synchrotron Radiation Facility, Shanghai Advanced Research Institute, Chinese Academy of Sciences, Shanghai 201204, China*

† Electronic supplementary information (ESI) available. See DOI: 10.1039/c9sc06574a

solutions can simultaneously assist crystallization of black-phase $CsPbI_3$ and improve the phase stability. However, these additives usually lead to low crystallization quality as revealed by the formation of small and disordered grains with sizes of tens of nanometers.[27,29] Therefore, developing a facile low-temperature processing route that can produce black-phase $CsPbI_3$ thin films with high crystallization quality and satisfactory phase stability is urgently required.

In this work, we report the realization of this goal by using a neutral molecular additive of 4(1*H*)-pyridinethione (4-PT) in the precursor solution of $CsPbI_3$. The additive is capable of assisting black-phase $CsPbI_3$ formation at 90–100 °C. The resulting $CsPbI_3$ thin films are morphologically uniform and phase stable under ambient conditions, consisting of micron-sized grains with oriented crystal stacking. Using a range of intermolecular interaction studies, the electron-enriched thione group in 4-PT is found to be critical in enabling a strong Pb–S interaction, which not only manipulates the crystallization paths, but also stabilizes the black-phase $CsPbI_3$ *via* crystal surface functionalization. Fully low-temperature processed $CsPbI_3$ solar cells exhibit a promising efficiency of 13.88% and a considerably high stability.

Results and discussion

4-PT enabled low-temperature formation of black-phase $CsPbI_3$ thin films with high crystallization quality and favorable phase stability

The $CsPbI_3$ perovskite films were fabricated *via* a simple one-step spin-coating method. As illustrated in Fig. 1a, the precursor solutions consisting of stoichiometric CsI and PbI_2 in a mixed solvent of DMF/DMSO, with or without the additive of 4-PT, were spin-coated onto a glass substrate at room temperature. Then the spin cast films were thermally annealed at a mild temperature of 90–100 °C for 5–10 minutes. We found that the additive-free sample exhibited a meta-stable dark intermediate at the beginning of annealing, but it quickly turned to a yellow film as shown in Fig. 1b. The occurrence of the transient dark state might be related to a solvent mediated reorganization of the precursor components. In contrast, the 4-PT based precursor film remained yellow during the first few minutes, and then slowly turned to black. Interestingly, the spontaneous phase transition from black to yellow was found to be suppressed in this sample, resulting in a stable black-phase $CsPbI_3$ film even at room temperature (Fig. 1b). We note that the widely used HI is not employed in our perovskite precursor solution, suggesting that 4-PT is effective in growing and stabilizing black-phase $CsPbI_3$ at a low temperature.

Fig. 1c shows the absorption spectra of the $CsPbI_3$ films fabricated with or without 4-PT. The 4-PT based film has an absorption cut-off at around 720 nm, corresponding to an optical bandgap of 1.73 eV. The photoluminescence (PL) spectrum of the black-phase $CsPbI_3$ film exhibits a single emission peak at about 715 nm (Fig. S1 in the ESI†). These optical data suggest that the 4-PT based film can be assigned to a so-called γ-phase $CsPbI_3$.[30] The additive-free yellow $CsPbI_3$ film shows limited visible-light absorption, with a PL peak at 415 nm (Fig. S2 and S3†). The absorption onset and PL peak wavelength are almost the same as those of the additive-free high-temperature annealed $CsPbI_3$ films (Fig. S4†). The X-ray diffraction (XRD) pattern of the 4-PT based $CsPbI_3$ film shows major peaks at 14.3° and 28.9° (Fig. 1d), which can be assigned

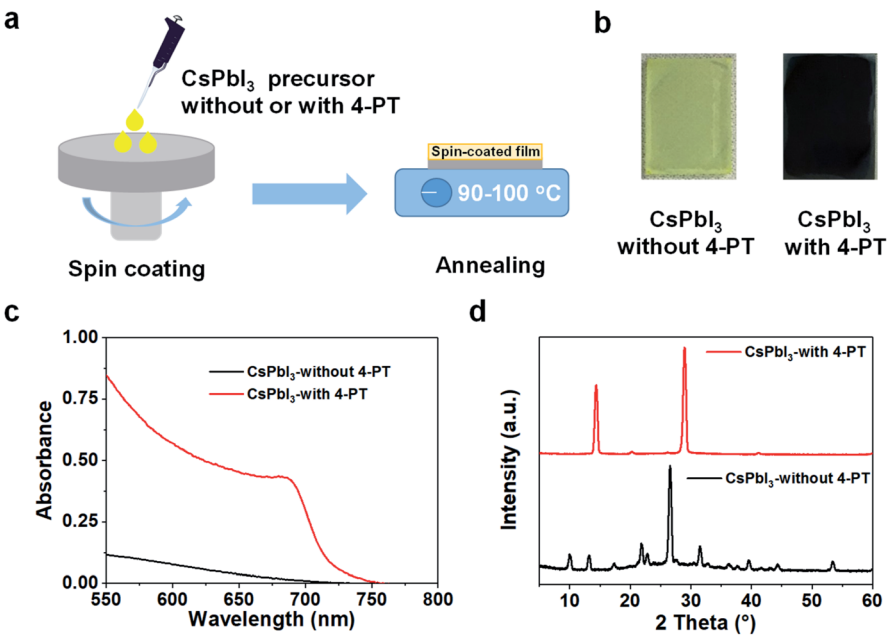

Fig. 1 Fabrication and characterization of $CsPbI_3$ films. (a) Schematic illustration of the fabrication process of $CsPbI_3$ films. (b) Photos of $CsPbI_3$ films prepared without or with the 4-PT additive after annealing at 90–100 °C for 10 minutes. (c) Absorption spectra and (d) XRD patterns of $CsPbI_3$ films without or with 4-PT.

to the (110) and (220) crystal planes of γ-phase $CsPbI_3$, respectively.[31] We note that the XRD pattern is very simple, indicating that the 4-PT molecules have not been intercalated into the perovskite crystal lattice. In contrast, the additive-free film exhibits characteristic diffraction peaks of δ-phase $CsPbI_3$.[32] All these UV-vis spectra and XRD patterns demonstrate that the neutral molecular additive of 4-PT is capable of low-temperature production and stabilization of black-phase $CsPbI_3$ thin films *via* a simple solution process.

The morphology of $CsPbI_3$ films fabricated with different concentrations of 4-PT in the precursor solution was studied by top-view scanning electron microscopy (SEM). Without the 4-PT additive, the yellow-phase $CsPbI_3$ film has a rough surface, large grains and large pinholes (Fig. 2a, left and Fig. S5†). Upon incorporation of 4-PT, the film quality is significantly improved. With the addition of 5 wt% 4-PT, the black-phase $CsPbI_3$ film has a smoother surface, but still contains a high density of small pinholes (Fig. S5†). The best film quality is obtained with a $CsPbI_3$ precursor solution containing 10 wt% 4-PT (Fig. 2a, right and Fig. S5†). It has a uniform surface, micron-sized grains and pinhole-free morphology. This type of dense film with large grains is desirable since there are fewer grain boundaries that could cause non-radiative recombination or moisture-induced crystal collapse.[33,34] Energy dispersive spectrometry (EDS) elemental mapping was used to determine the 4-PT distribution in the $CsPbI_3$ perovskite film. As shown in Fig. S6,† the characteristic C related to the organic molecules of 4-PT can be clearly detected on the surface and mainly concentrates at grain boundaries, whereas the Pb originating from perovskite exhibits homogeneous distribution on the surface. It has been demonstrated in XRD patterns that 4-PT would not enter the $CsPbI_3$ lattice; thus the added 4-PT is mainly located at the surface and grain boundaries. A higher concentration of 4-PT (15 wt%) does not lead to further improvement in the film morphology as revealed by the rough surface (Fig. S5†). Therefore, 10 wt% 4-PT is optimal for the nucleation and growth of the black-phase $CsPbI_3$ film, and the following tests are based on the optimum 4-PT concentration.

The time-resolved photoluminescence (TRPL) spectra in Fig. 2b show that the carrier lifetime of γ-$CsPbI_3$ stabilized by 4-PT is 338.95 ns, which is so far one of the longest PL lifetimes of $CsPbI_3$ perovskite, suggesting a high crystallization quality.[35] In contrast, the PL decay for the δ-$CsPbI_3$ film exhibits a short lifetime of 1.30 ns (Fig. 2b). Grazing-incidence wide-angle X-ray scattering (GIWAXS) analysis using synchrotron radiation was performed to study the crystalline orientation of the $CsPbI_3$ perovskite film. As shown in Fig. 2c, intense diffraction spots in the q_z direction with negligible spread along the Debye–Scherrer ring are observed. These results indicate that the crystal packing is highly oriented with a preferred out-of-plane orientation,[36] which is advantageous to the vertical direction charge transport in complete solar cells. The improved film morphology and crystalline quality can be attributed to the 4-PT modulated nucleation and crystal growth processes.[37,38] We note that in the presence of 4-PT, the crystallization of $CsPbI_3$ becomes very slow as no obvious XRD peaks can be observed even after annealing at 50 °C for 5 minutes (Fig. S7†). These results indicate that crystallization is greatly retarded during the

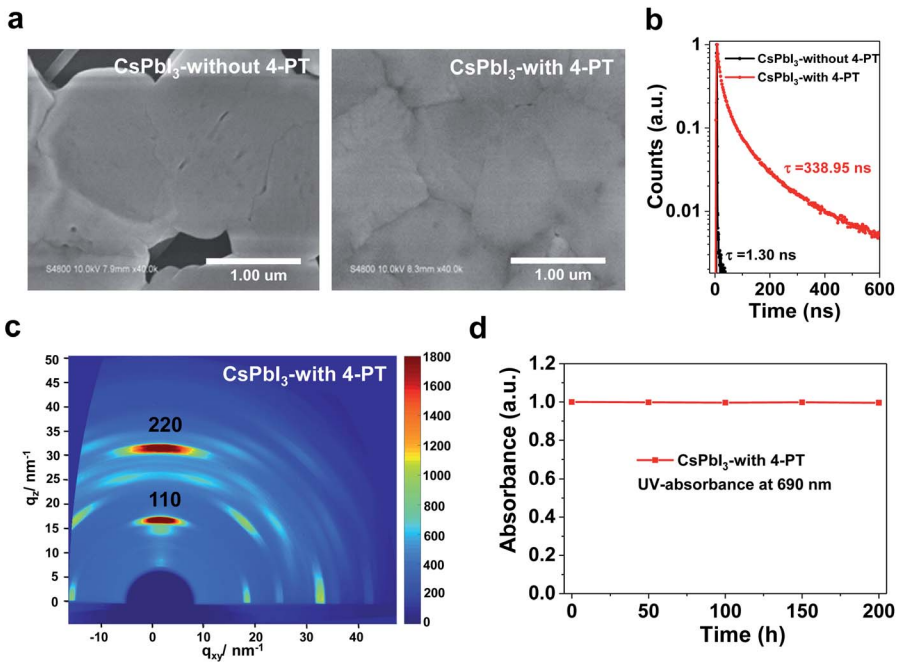

Fig. 2 Room temperature stabilized $CsPbI_3$ showing uniform morphology with high crystalline quality. (a) SEM images of $CsPbI_3$ films without or with 10 wt% 4-PT. (b) Time-resolved photoluminescence (TRPL) spectra of δ-$CsPbI_3$ and γ-$CsPbI_3$ films deposited on glass substrates. The excitation wavelength was fixed at 372 nm, and the emission wavelengths were set at 415 and 715 nm for $CsPbI_3$ films without and with 4-PT, respectively. (c) Grazing-incidence wide-angle X-ray scattering (GIWAXS) image for γ-$CsPbI_3$ stabilized by 4-PT. (d) Evolution of the absorbance at 690 nm for the 4-PT based $CsPbI_3$ film exposed to air (~20% RH).

supersaturation and film formation processes. The retardation of crystallization can be due to the strong coordination between highly polar thione ligands of 4-PT and Pb^{2+} ions, which will be verified later. Remarkably, the $CsPbI_3$ perovskite film with 4-PT could remain in the black phase after exposure to air at 20% humidity for over a week as evidenced by the unchanged UV-absorbance at 690 nm (Fig. 2d), indicating excellent air stability. It also shows high thermal stability as revealed by an acceleration test at 80 °C in a N_2 atmosphere (Fig. S8†). For comparison, we also fabricated additive-free (320 °C annealing for 10 min) and HI based black-phase $CsPbI_3$ films according to the literature[17] and evaluated their air stability under the same conditions as those for the 4-PT based samples. As shown in Fig. S9,† although the phase transition still exists in $CsPbI_3$ films with the 4-PT additive, the air stability is significantly improved when compared to those of the black-phase $CsPbI_3$ films generated by previous methods. These results indicate that a suitable modification of the crystallization modulation as well as surface functionalization is promising for overcoming the phase stability issues of $CsPbI_3$ perovskite.

All the above characterization results clearly reveal that 4-PT is a bi-functional additive that first modulates the crystallization paths to promote high-quality black phase $CsPbI_3$ formation and then passivates the crystal/film surface to enhance the ambient phase stability. As far as we know, this is the first time that low-temperature processed micro-sized black-phase $CsPbI_3$ was stabilized under ambient conditions for a long period, suggesting unique functions of the molecular additive of 4-PT.

Strong Pb–S interactions for crystallization path regulation and surface functionalization

To understand the impact of the additive 4-PT on $CsPbI_3$ crystallization, we first analyzed the crystallization paths as well as the phase transitions as shown in Fig. 3a. According to our observation of the additive-free sample, we estimate that the solvent involved CsI–PbI_2 mixed precursor film can pass through two different reaction paths at room temperature (RT): path-1 resulting in a thermodynamically stable yellow phase (non-perovskite δ-$CsPbI_3$); path-2 leading to the formation of metastable black phase (generally recognized as β- or γ-$CsPbI_3$).[15,21] According to the literature, these two paths have similar reaction energy barriers and usually coexist in a competitive state. However, upon mild heating (50–100 °C), the metastable black phase will easily turn into the yellow phase (path-3) by energetically overcoming its saddle point (Fig. 3a, right).[15] Once the yellow phase is formed, it will need a much higher annealing temperature (~320 °C) to recover to the black phase as shown by path-4 in Fig. 3a. Thus, the key issue for the formation of a stable black phase $CsPbI_3$ perovskite at low temperatures is to efficiently suppress path-1 and path-3.

Based on the above analysis, we further investigated the role of 4-PT in the crystallization process of $CsPbI_3$ perovskite. Firstly, the XRD patterns were compared for the samples of unheated $CsPbI_3$ precursor films with and without 4-PT. In the spun film without any additive (Fig. 3c), typical XRD peaks of δ-phase $CsPbI_3$ can be observed, verifying the fast formation of δ-phase $CsPbI_3$ at room temperature. In contrast, the unheated 4-PT based $CsPbI_3$ films are amorphous without any clear XRD peaks (Fig. 3c), suggesting that the presence of 4-PT can successfully inhibit the formation of δ-phase $CsPbI_3$ through path-1. In this case, the formation of black-phase $CsPbI_3$ *via* path-2 becomes more favorable. We speculated that the heteroatoms in 4-PT, including S and N that both have lone pair electrons and coordination capability with Pb^{2+}, should account for the retardation of δ-phase $CsPbI_3$ formation. To distinguish which heteroatom is more important, we first tried to use heterocycles like pyridine and piperidine that have only the N heteroatom to replace the 4-PT in the $CsPbI_3$ precursor solution and found that these additives can't suppress the formation of δ-phase $CsPbI_3$ at room temperature (Fig. S10†). According to the matching rules for Lewis acid–base adduction, sulfur is a soft base that should form more stable coordination with the soft acid of Pb^{2+}. Moreover, as shown in previous work,[39] the unique resonance structures of 4-PT may involve the lone pair electrons of nitrogen in the aromatic system, thus decreasing its coordination capability. Therefore, we considered that the heteroatom S involved thione group in 4-PT plays a more important role in affecting the crystallization of $CsPbI_3$.

As a proof-of-concept, a series of sulfur-containing additives (Fig. 3b) are incorporated into $CsPbI_3$ precursor solutions. Interestingly, we find that all of the unheated $CsPbI_3$ precursor films fabricated with additives containing the thione group are amorphous without any clear XRD peaks, while the thioether and thiophenol based samples exhibit obvious δ-phase $CsPbI_3$ peaks (Fig. 3c). These results demonstrate that the C=S functional group is unique in suppressing the formation of δ-phase $CsPbI_3$ at room temperature.

Upon heating at 90–100 °C for 10 minutes, the thioether and thiophenol based samples don't result in black-phase $CsPbI_3$ (Fig. S11†), which is not surprising as the already formed δ-phase $CsPbI_3$ can't be converted to the black phase (path-4) in this temperature range. In contrast, the 4-PT and *N*-methyl-4-PT based samples successfully turn black, and the black films are stable during long term storage in a glovebox (Fig. S11†). Unexpectedly, the sulfamide and thiourea based samples also can't result in black-phase $CsPbI_3$ after heating (Fig. S11†), although they are capable of suppressing the δ phase formation in precursor films at room temperature. These results indicate that the capability of suppressing the transition of black-phase $CsPbI_3$ to δ-phase $CsPbI_3$, *i.e.* path-3, is different for these C=S involved compounds, and only the pyridenethiones function well in this series of sulfur containing molecules.

To understand such a difference, we calculated the distribution of electrostatic potential (ESP) over these molecules by the density functional theory (DFT) method (Fig. 3b) and found that the ESP values around the S atom are negative and decrease in the sequence of thiophenol ≥ thioether > sulfamide > thiourea > 4-PT ≥ *N*-methyl-4-PT. The significant difference in ESP values for the C=S groups in sulfamide, thiourea, 4-PT and *N*-methyl-4-PT can be rationalized by molecular resonance formula analysis (see Notes in the ESI†). The negative ESP values mean enriching of electrons around the S atom, which may enhance the Pb–S coordination for modulation of the $CsPbI_3$ crystallization.

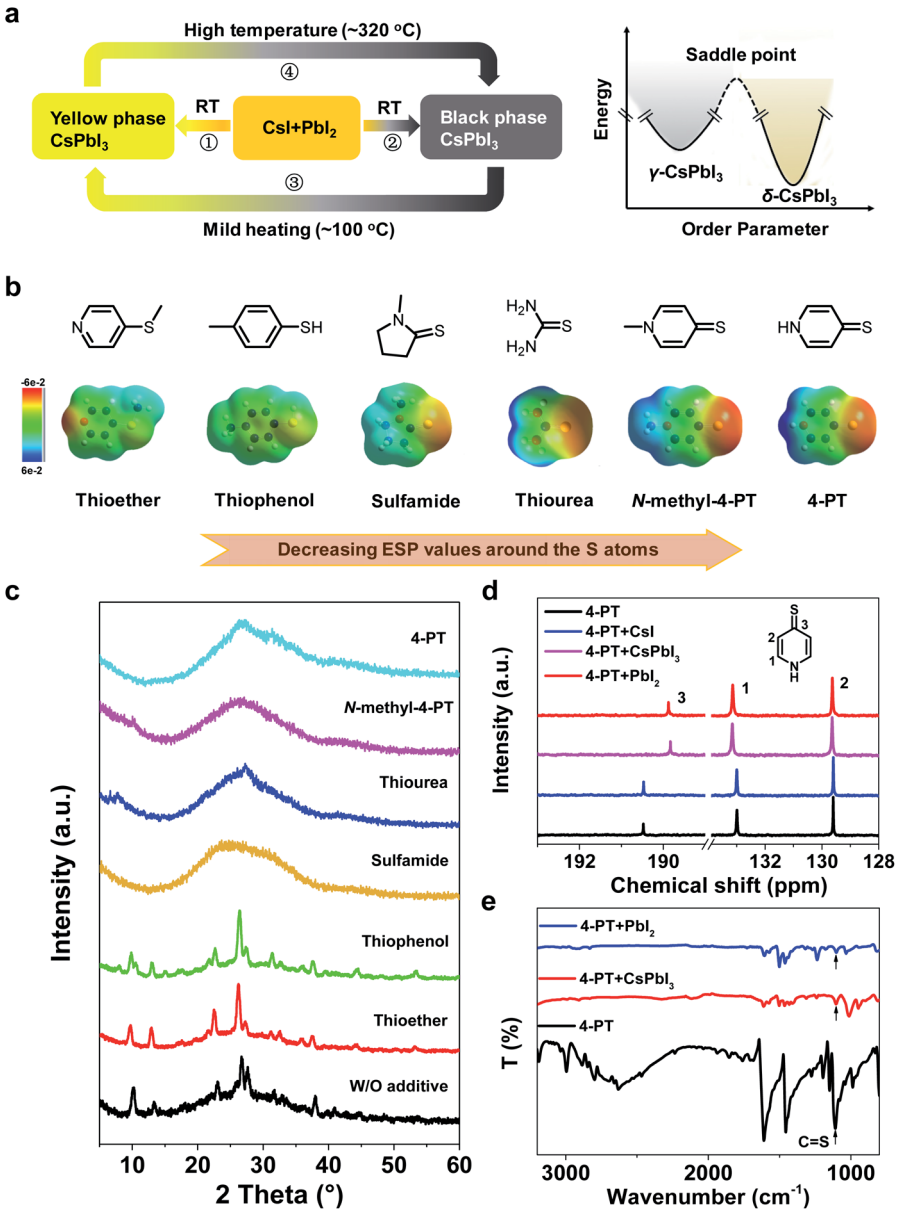

Fig. 3 Insight into the intermolecular interactions. (a) Left: schematic routes of $CsPbI_3$ phase transitions. Right: energy diagram indicating the relative stability of the black and yellow phases. (b) Chemical structures and corresponding calculated electrostatic potential (ESP) profiles of different additives. (c) XRD patterns of the perovskite precursor spun films without or with different additives before thermal annealing. (d) ^{13}C nuclear magnetic resonance (NMR) spectra of the pure 4-PT sample and 4-PT mixed with PbI_2, CsI and $CsPbI_3$ in DMSO-d_6 solution. (e) Fourier transform infrared (FTIR) spectra of pure 4-PT, $CsPbI_3$ and PbI_2 precursor films mixed with 4-PT.

Therefore, the most negative S atoms in pyridenethiones among this series of molecules, which lead to the strongest Pb–S coordination, should be responsible for their unique functionalities of growing and stabilizing black-phase $CsPbI_3$ by suppressing both path-1 and path-3 at low temperatures.

The molecular interactions between 4-PT and $CsPbI_3$ were further studied by nuclear magnetic resonance (NMR) in solution and Fourier transform infrared (FTIR) spectroscopy as well as Raman spectroscopy in thin films states. Fig. 3d shows the ^{13}C NMR spectra of pure 4-PT and a mixture of 4-PT with PbI_2, CsI or $CsPbI_3$ in deuterated dimethylsulfoxide (DMSO-d_6). There are only three peaks for pure 4-PT at different chemical shifts (δ) of 190.4, 133.0 and 129.6 ppm, corresponding to the *para*-(C_3), *ortho*-(C_1) and *meta*-(C_2) carbon atoms (relative to the N atom as shown in the inset), respectively. The very high chemical shift value of C_3 verifies the stable thione (C=S) structure in the DMSO solution. When the 4-PT is mixed with CsI, its ^{13}C NMR spectrum does not change, suggesting negligible molecular interactions between 4-PT and Cs^+ or I^- in DMSO. In contrast, a significant shift can be observed for the C_3 peak when 4-PT is mixed with PbI_2 or $CsPbI_3$, indicating that 4-PT mainly interacts with Pb^{2+} in the solutions *via* its thione group. The corresponding ^1H NMR spectra were recorded and are shown in Fig. S12,† showing a similar variation trend.

Fig. 3e shows the FTIR spectra of pure 4-PT and PbI_2 or $CsPbI_3$ films fabricated with the addition of 4-PT in precursor solutions. The broad band for pure 4-PT in the range of 2400–3000 cm^{-1} can be attributed to the intermolecular hydrogen bond of N–H···S.[40] This broad band disappears when 4-PT is mixed with PbI_2 or $CsPbI_3$ in their unheated films. Besides, the stretching vibration of C=S appearing at 1109 cm^{-1} for pure 4-PT is shifted to 1103 cm^{-1} upon contact with Pb^{2+} (Fig. 3e and S13†).[41] In the Raman spectroscopy measurement (Fig. S14†), we can clearly see that the typical Raman bands of PbI_2 (75, 96, 112, and 164 cm^{-1}) vanish and new bands at 154 and 205 cm^{-1} that can be assigned to the Pb–S bond appear for $CsPbI_3$ with the 4-PT complex.[42,43] The intense and sharp band associated with C–S stretching vibration (721 cm^{-1}) in the 4-PT sample becomes extremely weak and red-shifts to 715 cm^{-1} with the addition of $CsPbI_3$.[44] These results further confirm that the sulfur atom in 4-PT mainly reacts with perovskite *via* coordination.

Best performance of fully low-temperature processed $CsPbI_3$ planar p–i–n structured solar cells

To investigate the photovoltaic performance of the 4-PT-stabilized $CsPbI_3$ films, fully low-temperature processable planar p–i–n structured solar cells are fabricated by using poly [bis(4-phenyl)(2,4-dimethylphenyl)amine] (PTAA) and [6,6]-phenyl-C61-butyric acid methyl ester (PCBM) as the hole- and electron-transporting layer, respectively (Fig. S15†). The details of device fabrication can be found in the Experimental procedures. Fig. 4a shows the typical photocurrent density–voltage (*J–V*) curves of the solar cells. It can be seen that the additive-free δ-$CsPbI_3$ based device is almost short-circuited, showing a very low PCE of 0.007% with an open circuit voltage (V_{OC}) of 0.05 V, a short-circuit current density (J_{SC}) of 0.21 mA cm^{-2}, and a fill factor (FF) of 25.10%. In contrast, the performance is significantly enhanced for devices using 4-PT based perovskite as the active layer, which can mainly be attributed to the formation of a high-quality continuous thin film of black-phase $CsPbI_3$ (Fig. S16†). As shown in Fig. 4a, the best performing $CsPbI_3$ device stabilized by 10 wt% 4-PT exhibits a V_{OC} of 1.08 V, a J_{SC} of 17.38 mA cm^{-2}, an FF of 73.67% and a high PCE of 13.88% when measured under the reverse voltage scan. A similar PCE is achieved for the device measured under the forward voltage scan, indicating faint hysteresis in the devices. The cross sectional SEM image of the solar cell architecture is shown in Fig. S17.† A compact and fully covered perovskite layer with a thickness of about 300 nm can be observed. Moreover, the photocurrent density studied near the maximum power point shows a stable output, with a J_{max} of 15.04 mA cm^{-2} and a stabilized PCE of 13.54% (Fig. S18†), consistent with the values from the *J–V* curve. As shown in Fig. 4b, the incident photo-to-electron conversion efficiency (IPCE) spectrum of the best performing solar cell based on γ-$CsPbI_3$ exhibits a broad plateau, which is consistent with the absorption spectrum. The integrated J_{SC} is in good agreement with the current density acquired from the *J–V* curve. The statistics of PCE distribution shown in Fig. 4c demonstrate good reproducibility for this fabrication route. We further monitored the stability of the best-performing device in an ambient environment with encapsulation. As shown in Fig. 4d, the device retains over 85% of its original efficiency after storage in air for over 20 days. Both efficiency and stability achieved in this work are the best results among fully low-temperature processed $CsPbI_3$ photovoltaics.

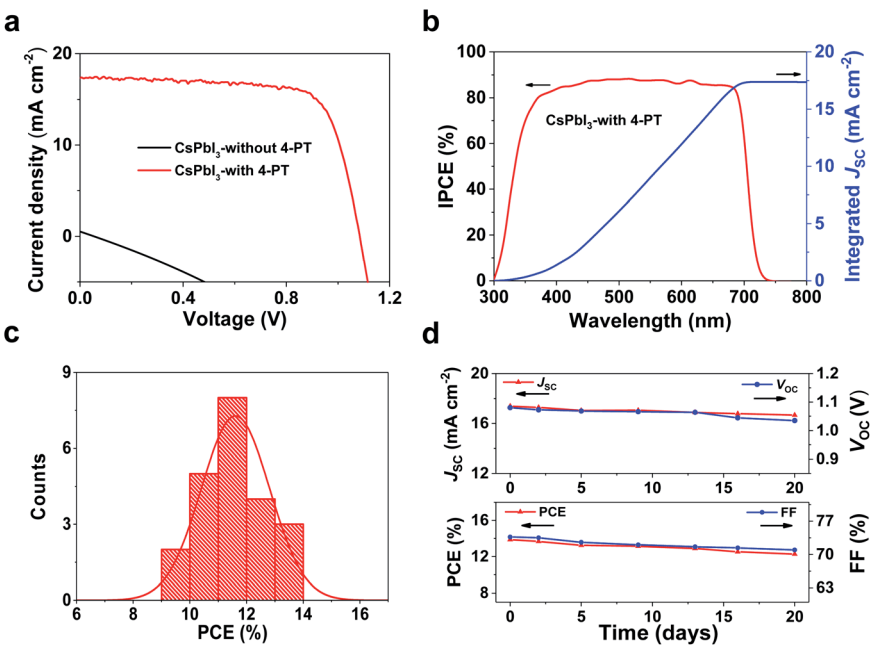

Fig. 4 Device performance and stability. (a) *J–V* curves of the $CsPbI_3$ devices. (b) The incident photon-to-current efficiency (IPCE) spectrum and corresponding integrated J_{SC} of solar cells based on γ-$CsPbI_3$ with 10 wt% 4-PT. (c) Histogram of device efficiencies for 20 devices of γ-$CsPbI_3$. (d) Stability test of the encapsulated device in an ambient environment.

Conclusions

In summary, we have demonstrated a successful low-temperature route to effectively prepare and stabilize black-phase $CsPbI_3$ by using a neutral molecular additive of 4(1*H*)-pyridinethione (4-PT). The electron-enriched thione group in 4-PT enables a strong Pb–S interaction, which not only influences the crystallization paths, but also stabilizes the black-phase $CsPbI_3$. It can effectively inhibit the formation of yellow δ-$CsPbI_3$ at room temperature, thus benefiting the formation of the black phase without high temperature annealing. After targeted crystallization, the *in situ* formed surface functionalization layer of 4-PT further stabilizes the black-phase $CsPbI_3$. The resulting $CsPbI_3$ thin films are morphologically uniform and phase stable under ambient conditions, consisting of micron-sized grains with oriented crystal stacking. All of the characterization results clearly reveal that 4-PT is a bi-functional additive that first modulates the crystallization paths to promote high-quality black phase $CsPbI_3$ formation and then passivates the crystal/film surface to enhance the ambient phase stability. As a result, a promising efficiency of 13.88% as well as excellent stability has been achieved, which are the best results for fully low-temperature processed p–i–n structured $CsPbI_3$ perovskite solar cells. This work provides a new avenue to design sulfur based additives for low-temperature processed high-quality and phase-stable $CsPbI_3$ thin films, which will be universally useful in the broad area of inorganic perovskite based optoelectronics.

Experimental procedures

Materials

The materials for perovskite solar cell fabrication were used as received, including lead(II) iodide (PbI_2, Kanto Chemical Co., Inc, Japan), cesium iodide (CsI, 99.9%, Alfa Aesar), poly[bis(4-phenyl) (2,4-dimethylphenyl)amine] (PTAA, M_w/M_n = 16 700/12 000, Derthon Optoelectronic Materials Science Technology Co., Ltd, China), poly[(9,9-bis(30-((*N*,*N*-dimethyl)-*N*-ethyl-ammonium)-propyl)-2,7-fluorene)-*alt*-2,7-(9,9-dioctylfluorene)] dibromide (PFNBr, Luminescence Technology Corp, China), [6,6]-phenyl-C61-butyric acid methyl ester (PCBM, Luminescence Technology Corp, China), and bathocuproine (BCP, >99%, Tokyo Chemical Industry Co., Ltd, Japan). The molecular additives used in the perovskite precursor solution were all purchased from TCI and Adamas-beta and used without further purification. *S*-methyl-4-mercaptopyridine and *N*-methyl-4-pyridinethione were synthesized as shown in the ESI. The super dehydrated solvents of dimethylsulfoxide (DMSO), *N*,*N*-dimethylformamide (DMF), chlorobenzene, and methanol were all purchased from Sigma-Aldrich.

Perovskite film fabrication

The $CsPbI_3$ precursor solution (0.8 M) was prepared by dissolving stoichiometric CsI and PbI_2 in a DMSO/DMF mixed solvent (v/v, 1/4). Different amounts of 4-PT (0%, 5%, 10%, and 15%, weight ratio to $CsPbI_3$) were added into the $CsPbI_3$ precursor solution. Then, the mixed perovskite precursor was stirred at 50 °C for 4 h. The precursor solution was spin coated on glass or PTAA/PFNBr coated glass/ITO substrates at a spin speed of 3000 rpm for 30 s and was annealed at 50 °C for 5 min, followed by annealing at 90–100 °C for 5–10 min to form the $CsPbI_3$ film.

Perovskite solar cell fabrication

The device fabrication was conducted in a glovebox with the oxygen level lower than 100 parts per million. Patterned indium tin oxide (ITO) glass was ultrasonically washed with detergent, deionized water, ethanol and acetone sequentially for 30 min. Before hole-transporting layer deposition, the substrates were further treated with ultraviolet ozone (UV-ozone) for 20 min. Then a compact layer of PTAA (2 mg ml^{-1}, chlorobenzene) was deposited on the ITO substrates (4000 rpm, 30 s) and annealed at 80 °C for 20 min. The PTAA film was further modified by PFNBr (0.5 mg ml^{-1} in methanol, 5000 rpm for 30 s) to increase the wetting properties of the perovskite precursor. After this, the $CsPbI_3$ active film was deposited by the process shown above. Next, a solution of PCBM dissolved in chlorobenzene (20 mg ml^{-1}) was spin coated on the perovskite layer at 10 00 rpm for 20 s and annealed at 80 °C for 30 min. Then, a layer of BCP (saturated solution in methanol) was deposited on top of the PCBM layer (6000 rpm, 30 s). Finally, a 100 nm silver counter electrode was prepared by thermal evaporation.

Characterization

The XRD spectra of inorganic perovskite films were recorded on a Rigaku Ultima IV (Cu Kα radiation, $\lambda = 1.5406$ Å) in the range of 5°–90° (2θ). The UV-vis absorption spectra and photoluminescence (PL) spectra were recorded on a Varian Cary 100 spectrophotometer and Horiba Fluoromax-4 fluorescence spectrometer, respectively. Photoluminescence lifetimes were determined using the single photon counting technique by means of an Edinburgh FLS890 spectrometer. The SEM images were characterized using a TESCAN VEGA 3 SBH scanning electron microscope. The fluorescence lifetime was determined using an Edinburgh FLS890 spectrometer with the single photon counting technique. The EDS mapping images were obtained by using a GeminiSEM 500 equipped with EDX. ^{13}C and ^{1}H NMR spectra were obtained with a Bruker AM 400 spectrometer. The FTIR and Raman spectra were obtained on a Tensor 27 FTIR spectrometer (Nicolet 6700) and a laser micro-Raman spectrometer (Renishaw in *via* Reflex), respectively. The photovoltaic performances (*J*–*V* curves) were analyzed using a Keithley 2400 Sourcemeter under standard AM 1.5 simulated solar irradiation (WXS-155S-10) and the solar cells were measured using a metal mask to make the active area around 0.09 cm^2. The incident photon-to-current efficiency (IPCE) measurements were conducted on a Newport-74125 system (Newport Instruments).

First-principles calculation

Geometry optimization and electronic properties of the additive molecules were computed using the Gaussian 09 program by

density functional theory (DFT) employing the B3LYP and Pople standard split-valence plus polarization 6-31G* basis set. The molecular electrostatic field distributions were visualized using GaussView.

Conflicts of interest

There are no conflicts to declare.

Acknowledgements

This work was financially supported by the NSFC/China (21706070, 21822504, 21788102 and 21421004), Shanghai Municipal Science and Technology Major Project (2018SHZDZX03), Program of Introducing Talents of Discipline to Universities (B16017), Eastern Scholar (TP2016018), Science and Technology Commission of Shanghai Municipality (17ZR1407400), China Association of Science and Technology (2017QNRC001) and the Fundamental Research Funds for the Central Universities (WJ1714007).

Notes and references

1 A. Kojima, K. Teshima, Y. Shirai and T. Miyasaka, *J. Am. Chem. Soc.*, 2009, **131**, 6050–6051.
2 W. Chen, Y. Wu, Y. Yue, J. Liu, W. Zhang, X. Yang, H. Chen, E. Bi, I. Ashraful, M. Grätzel and L. Han, *Science*, 2015, **350**, 944.
3 X. Sun, F. Wu, C. Zhong, L. Zhu and Z. Li, *Chem. Sci.*, 2019, **10**, 6899–6907.
4 Y. Wang and L. Han, *Sci. China: Chem.*, 2019, **62**, 822–828.
5 Q. Jiang, Y. Zhao, X. Zhang, X. Yang, Y. Chen, Z. Chu, Q. Ye, X. Li, Z. Yin and J. You, *Nat. Photonics*, 2019, **13**, 460–466.
6 G. Grancini, V. D'Innocenzo, E. R. Dohner, N. Martino, A. R. Srimath Kandada, E. Mosconi, F. De Angelis, H. I. Karunadasa, E. T. Hoke and A. Petrozza, *Chem. Sci.*, 2015, **6**, 7305–7310.
7 T. Leijtens, G. E. Eperon, N. K. Noel, S. N. Habisreutinger, A. Petrozza and H. J. Snaith, *Adv. Energy Mater.*, 2015, **5**, 1500963.
8 D. Yu, Y. Hu, J. Shi, H. Tang, W. Zhang, Q. Meng, H. Han, Z. Ning and H. Tian, *Sci. China: Chem.*, 2019, **62**, 684–707.
9 B. Park and S. I. Seok, *Adv. Mater.*, 2019, **31**, 1805337.
10 R. J. Sutton, G. E. Eperon, L. Miranda, E. S. Parrott, B. A. Kamino, J. B. Patel, M. T. Hörantner, M. B. Johnston, A. A. Haghighirad, D. T. Moore and H. J. Snaith, *Adv. Energy Mater.*, 2016, **6**, 1502458.
11 L. A. Frolova, D. V. Anokhin, A. A. Piryazev, S. Y. Luchkin, N. N. Dremova, K. J. Stevenson and P. A. Troshin, *J. Phys. Chem. Lett.*, 2016, **8**, 67–72.
12 M. Kulbak, S. Gupta, N. Kedem, I. Levine, T. Bendikov, G. Hodes and D. Cahen, *J. Phys. Chem. Lett.*, 2015, **7**, 167–172.
13 W. Ahmad, J. Khan, G. Niu and J. Tang, *Sol. RRL*, 2017, **1**, 1700048.
14 R. E. Beal, D. J. Slotcavage, T. Leijtens, A. R. Bowring, R. A. Belisle, W. H. Nguyen, G. F. Burkhard, E. T. Hoke and M. D. McGehee, *J. Phys. Chem. Lett.*, 2016, **7**, 746–751.
15 J. A. Steele, H. Jin, I. Dovgaliuk, R. F. Berger, T. Braeckevelt, H. Yuan, C. Martin, E. Solano, K. Lejaeghere, S. M. J. Rogge, C. Notebaert, W. Vandezande, K. P. F. Janssen, B. Goderis, E. Debroye, Y. Wang, Y. Dong, D. Ma, M. Saidaminov, H. Tan, Z. Lu, V. Dyadkin, D. Chernyshov, V. Van Speybroeck, E. H. Sargent, J. Hofkens and M. B. J. Roeffaers, *Science*, 2019, **365**, 679.
16 K. Wang, Z. Jin, L. Liang, H. Bian, D. Bai, H. Wang, J. Zhang, Q. Wang and S. Liu, *Nat. Commun.*, 2018, **9**, 4544.
17 G. E. Eperon, G. M. Paternò, R. J. Sutton, A. Zampetti, A. A. Haghighirad, F. Cacialli and H. J. Snaith, *J. Mater. Chem. A*, 2015, **3**, 19688–19695.
18 Y. Wang, T. Zhang, M. Kan and Y. Zhao, *J. Am. Chem. Soc.*, 2018, **140**, 12345–12348.
19 C. Liu, W. Li, C. Zhang, Y. Ma, J. Fan and Y. Mai, *J. Am. Chem. Soc.*, 2018, **140**, 3825–3828.
20 Y. Wang, M. I. Dar, L. K. Ono, T. Zhang, M. Kan, Y. Li, L. Zhang, X. Wang, Y. Yang, X. Gao, Y. Qi, M. Grätzel and Y. Zhao, *Science*, 2019, **365**, 591.
21 P. Wang, X. Zhang, Y. Zhou, Q. Jiang, Q. Ye, Z. Chu, X. Li, X. Yang, Z. Yin and J. You, *Nat. Commun.*, 2018, **9**, 2225.
22 W. Chen, H. Chen, G. Xu, R. Xue, S. Wang, Y. Li and Y. Li, *Joule*, 2018, **3**, 304.
23 H. Yuan, Y. Zhao, J. Duan, Y. Wang, X. Yang and Q. Tang, *J. Mater. Chem. A*, 2018, **6**, 24324–24329.
24 T. Zhang, M. I. Dar, G. Li, F. Xu, N. Guo, M. Grätzel and Y. Zhao, *Sci. Adv.*, 2017, **3**, e1700841.
25 Y. Wang, T. Zhang, M. Kan, Y. Li, T. Wang and Y. Zhao, *Joule*, 2018, **2**, 2065–2075.
26 B. Zhao, S. Jin, S. Huang, N. Liu, J. Ma, D. Xue, Q. Han, J. Ding, Q. Ge, Y. Feng and J. Hu, *J. Am. Chem. Soc.*, 2018, **140**, 11716–11725.
27 Q. Wang, X. Zheng, Y. Deng, J. Zhao, Z. Chen and J. Huang, *Joule*, 2017, **1**, 371–382.
28 B. Li, Y. Zhang, L. Fu, T. Yu, S. Zhou, L. Zhang and L. Yin, *Nat. Commun.*, 2018, **9**, 1076.
29 B. Jeong, H. Han, Y. J. Choi, S. H. Cho, E. H. Kim, S. W. Lee, J. S. Kim, C. Park, D. Kim and C. Park, *Adv. Funct. Mater.*, 2018, **28**, 1706401.
30 R. J. Sutton, M. R. Filip, A. A. Haghighirad, N. Sakai, B. Wenger, F. Giustino and H. J. Snaith, *ACS Energy Lett.*, 2018, **3**, 1787–1794.
31 Y. Zhao, Y. Wang, X. Liu, T. Zhang, X. Wang, M. Kan and J. Shi, *Angew. Chem., Int. Ed.*, 2019, **58**, 16691–16696.
32 A. Marronnier, G. Roma, S. Boyer-Richard, L. Pedesseau, J. Jancu, Y. Bonnassieux, C. Katan, C. C. Stoumpos, M. G. Kanatzidis and J. Even, *ACS Nano*, 2018, **12**, 3477–3486.
33 Z. Zeng, J. Zhang, X. Gan, H. Sun, M. Shang, D. Hou, C. Lu, R. Chen, Y. Zhu and L. Han, *Adv. Energy Mater.*, 2018, **8**, 1801050.
34 D. Ghosh, D. K. Chaudhary, M. Y. Ali, K. K. Chauhan, S. Prodhan, S. Bhattacharya, B. Ghosh, P. K. Datta, S. C. Ray and S. Bhattacharyya, *Chem. Sci.*, 2019, **10**, 9530–9541.

35 W. Zhang and W. Zhu, *Green Energy Environ.*, 2017, **2**, 67–69.
36 J. Rivnay, S. C. B. Mannsfeld, C. E. Miller, A. Salleo and M. F. Toney, *Chem. Rev.*, 2012, **112**, 5488–5519.
37 F. Wang, H. Yu, H. Xu and N. Zhao, *Adv. Funct. Mater.*, 2015, **25**, 1120–1126.
38 S. S. Mali, J. V. Patil, H. Kim, H. Kim and C. K. Hong, *Adv. Funct. Mater.*, 2019, **29**, 1807420.
39 H. Hanika-Heidl and R. D. Fischer, *Inorg. Chim. Acta*, 2004, **357**, 1748–1760.
40 X. Shi, R. Jiang, W. Song and B. Zhao, *Spectrosc. Spectral Anal.*, 2012, **32**, 1588–1591.
41 E. Spinner, *J. Chem. Soc.*, 1960, 1237–1242.
42 G. D. Smith, S. Firth, R. J. H. Clark and M. Cardona, *J. Appl. Phys.*, 2002, **92**, 4375–4380.
43 J. M. C. D. Silva Filho, V. A. Ermakov and F. C. Marques, *Sci. Rep.*, 2018, **8**, 1563.
44 J. Hu, B. Zhao, W. Xu, B. Li and Y. Fan, *Spectrochim. Acta, Part A*, 2002, **58**, 2827–2834.